C. R. Mecanique 346 (2018) 932–947

Contents lists available at ScienceDirect

Comptes Rendus Mecanique

www.sciencedirect.com

Jet noise modelling and control / Modélisation et contrôle du bruit de jet

Computational analysis of exit conditions on the sound field of turbulent hot jets

Mehmet Onur Cetin [a,*], Seong Ryong Koh [a], Matthias Meinke [a,b], Wolfgang Schröder [a,b]

[a] Institute of Aerodynamics, RWTH Aachen University, Wüllnerstraße 5a, 52062 Aachen, Germany
[b] Forschungszentrum Jülich, JARA – High-Performance Computing, 52425 Jülich, Germany

ARTICLE INFO

Article history:
Received 1 July 2017
Accepted 4 April 2018
Available online 16 August 2018

Keywords:
Large-eddy simulation
Acoustic perturbation equations
Jet aeroacoustics
Multi shear-layer flow

ABSTRACT

A hybrid computational fluid dynamics (CFD) and computational aeroacoustics (CAA) method is used to compute the acoustic field of turbulent hot jets at a Reynolds number $Re = 316,000$ and a Mach number $M = 0.12$. The flow field computations are performed by highly resolved large-eddy simulations (LES), from which sound source terms are extracted to compute the acoustic field by solving the acoustic perturbation equations (APE). Two jets are considered to analyze the impact of exit conditions on the resulting jet sound field. First, a jet emanating from a fully resolved non-generic nozzle is simulated by solving the discrete conservation equations. This computation of the jet flow is denoted free-exit-flow (FEF) formulation. For the second computation, the nozzle geometry is not included in the computational domain. Time averaged exit conditions, i.e. velocity and density profiles of the first formulation, plus a jet forcing in form of vortex rings are imposed at the inlet of the second jet configuration. This formulation is denoted imposed-exit-flow (IEF) formulation. The free-exit-flow case shows up to 50% higher turbulent kinetic energy than the imposed-exit-flow case in the jet near field, which drastically impacts noise generation. The FEF and IEF configurations reveal quite a different qualitative behavior of the sound spectra, especially in the sideline direction where the entropy source term dominates sound generation. This difference occurs since the noise sources generated by density and pressure fluctuations are not perfectly modeled by the vortex ring forcing method in the IEF solution. However, the total overall sound pressure level shows the same qualitative behavior for the FEF and IEF formulations. Towards the downstream direction, the sound spectra of the FEF and IEF solutions converge.

1. Introduction

The understanding of the acoustic field of propulsive jets is one of the most elusive problems in aeroacoustics, although impressive research results have been obtained over the last few decades. The jet near field and the dominant noise sources strongly depend on the flow conditions at the nozzle exit. In other words, the overall reliability of an acoustic prediction is defined by the quality of the jet inlet conditions, and an accurate determination of the acoustic field requires the computa-

* Corresponding author.
E-mail address: o.cetin@aia.rwth-aachen.de (M.O. Cetin).

https://doi.org/10.1016/j.crme.2018.07.006
1631-0721/

tion of the flow inside the nozzle. Zaman [1], for example, experimentally showed that two jets with the same nozzle exit diameter but different interior nozzle details can produce remarkably varying spectra.

However, to reduce the computational costs, it was common in the past to exclude the nozzle geometry from the computational domain. In those studies, usually artificial perturbations are imposed to prevent any spurious noise generation. The transition to a fully turbulent free-shear layer is initiated by synthetic fluctuations to obtain the correct spreading rate of the free-shear layer. Although highly developed inflow formulations exist, which are extremely useful for generic nozzle geometries, it is still questionable whether such inflow forcing methods yield an acceptably accurate sound field in the near field, i.e. sound pressure level distributions, directivity pattern etc., when technically relevant nozzle geometries are considered.

In a vast number of large-eddy simulation or direct numerical simulation studies, the effect of artificially forced inflow conditions on the development of cold jets was analyzed. Andersson et al. [2], for instance, exploited numerical data to determine the influence of the inflow conditions on the acoustic field. At a fixed Reynolds number, a jet with synthesized turbulence showed only a small change in the overall sound pressure level (OASPL) distribution compared to a jet without synthesized turbulence. Keiderling et al. [3] numerically studied the influence of inflow forcing on the flow and sound field of isothermal high subsonic jets. They introduced several instability modes to excite the jet turbulence. The amplitude of the inflow disturbances was changed in the range 1.5%, 3%, and 4.5% of the exit velocity. They reported that by increasing the forcing amplitude the low-frequency noise reduces. Moreover, they observed that, in the 3% and 4.5% amplitude cases, a tonal component at $St = 0.9$ occurs, which reduces the frequency where the decay of the SPL spectra occurs. Bogey and Bailly [4] numerically examined the effect of the flow state at the nozzle exit of initially laminar jets on the flow and the resulting acoustic field. They showed that the pairing noise was shifted to higher frequencies as the momentum thickness decreases. They also found a noticeable noise level reduction when random perturbations at the inlet section of the jet are imposed. Furthermore, Bogey and Marsden [5] numerically analyzed the impact of nozzle exit boundary layer thickness on the sound field of subsonic isothermal jets. The inflow distribution was excited by random vortical disturbances. They observed that for an increased boundary layer thickness, the noise level decreases due to the reduction of the turbulence intensities in the near sound field. Bodony and Lele [6] reviewed numerous jet studies being performed at various flow conditions. They concluded that the inflow forcing has a remarkable impact on the turbulence level and the sound field of the jet.

Other jet studies focused on hot flow conditions. Bodony and Lele [7] explored jets at heated and unheated flow conditions. Their results exhibited a lower noise level in the unheated jet at a low Mach number $M = 0.51$. It is known that heated transonic jets, i.e. $M > 0.7$, reduce the noise level, while the noise level is increased for high subsonic jets, $M < 0.7$, compared to the unheated jets at the same jet velocity [8]. Koh et al. [9] numerically investigated single and coaxial jets for hot and cold stream conditions. They showed that the low-frequency noise is enhanced by the pronounced temperature gradients that intensify the turbulent structures. The experimental results in [10] evidenced the dependence of the spectral shape of the acoustic field on the jet temperature, showing an extra hump in the frequency band. Furthermore, subsonic heated jets showed an enlargement of the maxima of the acoustic spectra at acute angles. Gloor et al. [11] numerically investigated the sound field of coaxial hot jets at various temperature ratios between the primary core and the secondary core. They reported, for a higher temperature of the primary core of the jet, an increase of the overall sound pressure level. Far-field measurements of high subsonic jets at varying fluid temperatures were analyzed in [12]. It was found that, at a constant Mach number, an increasing jet temperature decreases the high-frequency content of the noise spectra at shallow radiation angles.

Nozzles with built-in components create an internally mixed multi-shear-layer flow that increases the complexity of the flow state at the exit. The studies [13–17] showed the importance of the internal nozzle geometry upstream of the nozzle exit on the flow field, and thus on the jet noise. Recent efforts focused on the impact of the inner nozzle geometry on the exhaust plume and the resulting acoustic field. Fan flow deflectors, i.e. wedges, vanes etc., for example, are analyzed in [18–21]. Overall, it was found that nozzle built-in components can yield an acoustic shielding effect, i.e. the noise level is mitigated by an increased turbulent mixing in the jet near field. However, it has to be stated that, in the majority of the studies, in which large-eddy simulations or direct numerical simulations were performed, the influence of the nozzle geometry has not been discussed to avoid the enormous computational costs.

The investigation of the impact of the various nozzle exit formulations on the sound field is the purpose of this study. As stated above, previous studies mostly focused on single and coaxial jet flows by prescribing steady inflow distributions plus some perturbations to excite the nonlinear growth of the shear layer instabilities. A study in which the influence of the exit conditions from a realistic multiple shear layer generating nozzle flow on the acoustic field is analyzed is still missing. To investigate such a problem, a slightly simplified helicopter nozzle geometry, which generates an inner shear layer created by flow structures shedding from a centerbody and an outer shear layer from the nozzle lip, is considered.

Highly resolved numerical analyses for low Mach number turbulent hot jets are performed to determine the effect of exit conditions on the resulting acoustic field. The Reynolds number is $Re = 316,000$ and the Mach number is $M = 0.12$. Two jet setups are considered by large-eddy simulations (LES) that determine the sound source terms of the acoustic field, which is simulated by solving the acoustic perturbation equations (APE). In the first setup, the internal nozzle flow is computed so that the nozzle exit flow is determined by the LES solution of the conservation equations. This case is denoted free-exit-flow (FEF) formulation. In the second setup, the details of the flow inside the nozzle are not considered. This formulation is comparable to the standard approach in the literature. The time averaged flow distribution of the nozzle-jet

solution of the FEF case plus a jet forcing define the nozzle exit flow distribution, i.e. the inflow of the second jet analysis. This formulation is denoted imposed-exit-flow (IEF). The acoustic fields of the FEF and the IEF approach are compared.

The present article has the following structure. First, the numerical methods of the flow and acoustic computations are introduced. Then, the flow and acoustic problem setups of the two jet configurations are briefly described. Subsequently, the essential findings of the flow fields are concisely summarized, while the acoustic fields and the differences are discussed in detail. Finally, the essential results are summarized.

2. Numerical method

2.1. Flow field

The turbulent, unsteady, compressible flow field is determined by solving the Navier–Stokes equations using a massively parallelized unstructured Cartesian finite-volume cut-cell method. The large-eddy simulation is based on the monotone integrated large-eddy simulation (MILES) approach [22]. That is, the truncation error of the numerical scheme mimics the dissipation of the unresolved subgrid scales.

The convective fluxes of the governing equations are formulated by a low dissipation version of the advection upstream splitting method (AUSM) [23]. The cell center gradients for the second-order derivatives are computed using a second-order accurate least-squares reconstruction scheme [24] so that the overall spatial approximation is second-order accurate. An explicit second-order 5-stage Runge–Kutta method is used for the temporal integration of the conservation equations [25].

A Cartesian unstructured fully parallel mesh generator with hierarchical mesh refinement is used for the grid generation [26]. In the vicinity of the boundaries, the equidistant cells are reshaped into cut cells [24], where fully conservative boundary conditions are applied. Small cut-cells are treated using an interpolation and flux-redistribution method developed by Schneiders et al. [25,27]. Further details of the numerical methods are described by Meinke et al. [23] and Hartman et al. [24]. This solution method has been validated for several internal and external flow problems such as various jet flows, axial fan flows, premixed flames, etc. [28–30].

At the inflow boundaries of the flow problems, a zero-pressure gradient normal to the inlet plane is prescribed. Adiabatic no-slip conditions with a zero-pressure gradient are imposed on the walls. For the outflow and lateral boundary conditions, a constant static pressure is prescribed and all other variables are extrapolated along linearized characteristics from the interior domain. To prevent spurious reflections from the boundaries, sponge layers are prescribed [31].

2.2. Acoustic field

The acoustic perturbation equations (APE) are applied to determine the sound propagation and to identify the dominant noise sources. Since a compressible flow problem is considered, the APE-4 system is used [32]. The acoustic perturbation equations were derived from the continuity and Navier–Stokes equations. Using an expression for the excess density $\rho_e = (\rho - \overline{\rho}) - (p - \overline{p})/\overline{a^2}$, where the overbar denotes mean quantities, the rearranged APE-4 system [33] reads

$$\frac{\partial p'}{\partial t} + \overline{a^2}\nabla \cdot \left(\overline{\rho}\mathbf{u}' + \overline{\mathbf{u}}\frac{p'}{\overline{a^2}} \right) = \overline{a^2}(q_c + q_e) \tag{1}$$

$$\frac{\partial \mathbf{u}'}{\partial t} + \nabla\left(\overline{\mathbf{u}} \cdot \mathbf{u}'\right) + \nabla\left(\frac{p'}{\overline{\rho}}\right) = \mathbf{q}_m \tag{2}$$

The right-hand side source terms are

$$q_c = -\nabla \cdot \left(\rho'\mathbf{u}'\right)' \tag{3}$$

$$q_e = \underbrace{-\frac{\partial \rho_e}{\partial t}}_{q_{et}} \underbrace{-\nabla \cdot (\rho_e \overline{\mathbf{u}})}_{q_{es}} \tag{4}$$

$$\mathbf{q}_m = -(\omega \times \mathbf{u})' - \left(\nabla \frac{|\mathbf{u}'|^2}{2}\right)' + \nabla\frac{p'}{\overline{\rho}} - \left(\frac{\nabla p}{\rho}\right)' \tag{5}$$

The excess density represents the difference between the density and the pressure perturbation at an analogous acoustic medium whose density perturbation is isentropic, and the sound speed is a [34].

The first step of the hybrid method is based on an LES for the turbulent jet flow to provide the data of the noise source terms in Eqs. (3), (4), and (5). Then, the corresponding acoustic field is computed by solving the acoustic perturbation equations (1) and (2).

To accurately resolve the acoustic wave propagation, a 6th-order dispersion-relation-preserving finite-difference scheme [35] is used for the spatial discretization and an alternating 5–6-stage low-dispersion and low-dissipation Runge–Kutta method for the temporal integration [36]. On the embedded boundaries between the inhomogeneous and the homogeneous acoustic domain, a damping zone has been implemented to suppress spurious sound generated by the

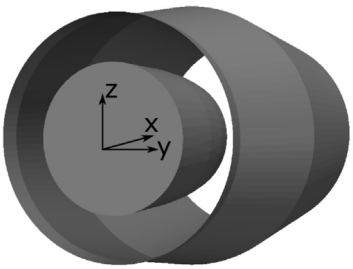

Fig. 1. Rear section of the nozzle geometry and coordinate system. The x-direction defines the streamwise direction.

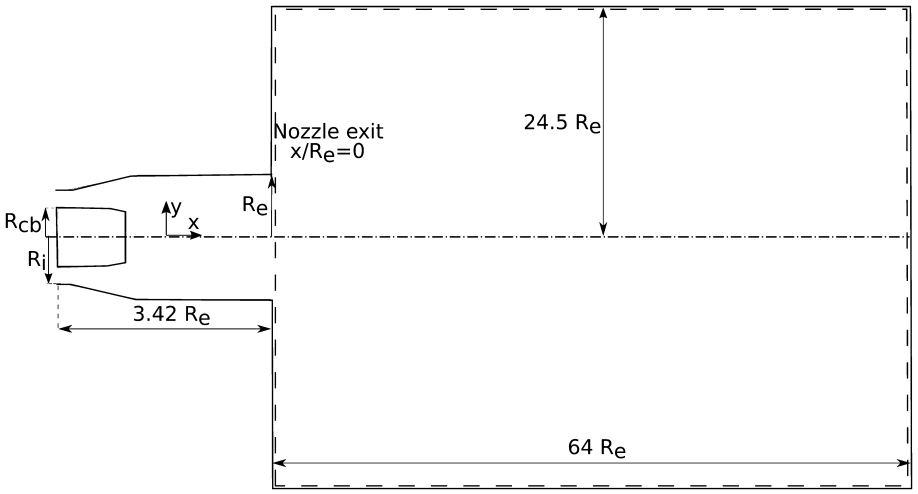

Fig. 2. Sketch of the computational domain of the flow fields for the FEF (—) and the IEF case (– –).

acoustic-flow-domain transition [37]. A detailed description of the two-step method and the discretization of the Navier–Stokes equations and the acoustic perturbation equations is given in [38].

For the acoustic computations, non-reflecting boundary conditions [35] are prescribed on the boundaries of the computational domain.

3. Problem definition and computational mesh

3.1. Flow field

Fig. 1 illustrates the interior of the divergent annular axisymmetric nozzle used in the LES computation of the FEF case. The details of the nozzle geometry and the extent of the computational domains of the FEF and the IEF case are given in Fig. 2. The quantity R_i is the nozzle inlet radius, R_{cb} the radius of the centerbody, and R_e the nozzle exit radius. The nozzle expansion ratio R_e/R_i is 1.3125 and the ratio of the radii of the centerbody and the exit cross section R_{cb}/R_e is 0.42.

As stated before, two computational setups are considered. For the free-exit-flow (FEF) configuration, in which the flow inside the nozzle is computed, isotropic synthetic turbulence is superimposed to the steady flow field at the inflow plane with 10% turbulence intensity. Note that the inflow plane is located $3.42\,R_e$ upstream of the nozzle exit (Fig. 2). This synthetic turbulence generation method is only used to prescribe the inflow distribution for the FEF configuration. The method that yields a divergence-free velocity distribution is described in detail in [39].

The inflow plane of the imposed-exit-flow (IEF) configuration matches the exit cross section of the nozzle (Fig. 2). To trigger the growth of the instabilities of the free-shear layer shed from the centerbody and the wall-bounded shear layer, two distinct vortex rings are prescribed for the inner ($r/R_e \approx 0.45$) and the outer ($r/R_e \approx 1$) shear layer.

The axial and radial vortex ring velocities are

$$U_{ax,ring} = \frac{2r_{ring}}{r\triangle y}\exp\left(-\ln(2)\frac{\triangle(x,r)^2}{(\triangle y)^2}\right)(r - r_{ring}) \tag{6}$$

$$V_{rad,ring} = \frac{2r_{ring}}{r\triangle y}\exp\left(-\ln(2)\frac{\triangle(x,r)^2}{(\triangle y)^2}\right)(x - x_{ring}) \tag{7}$$

Table 1
Coefficients of the velocity distribution of Eq. (10).

Coefficient	a_0	a_1	a_2	a_3	a_4	a_5
IEF u(r)	0.0037333	0.22194	−0.20494	2.1886	−70.185	−8.3139
Coefficient	a_6	a_7	a_8	a_9	a_{10}	
IEF u(r)	208.9	7.0968	10.165	−206.51	0.11101	

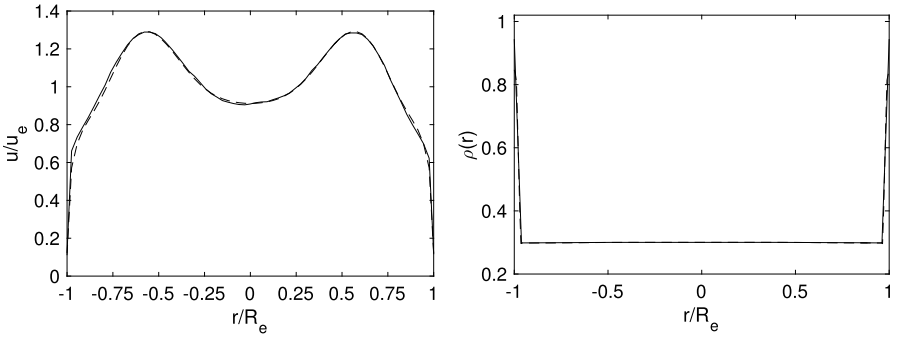

(**a**) (**b**)

Fig. 3. (a) Axial velocity, (b) density distributions of the jets for (—) FEF, (−−) IEF. The distributions of the FEF solution is obtained by time averaging the solution at the nozzle exit, whereas the IEF solution is determined by a 10th-order polynomial fit and the Crocco–Busemann relation.

where r_{ring} and x_{ring} are the ring radius and the axial position. Using the thickness of the ring in the axial and radial direction, i.e. $x - x_{\text{ring}}$ and $r - r_{\text{ring}}$, the quantity $\triangle(x,r)^2$ is defined $\triangle(x,r)^2 = (x - x_{\text{ring}})^2 + (r - r_{\text{ring}})^2$ and $\triangle y$ is the grid spacing in the y-direction. Note that the vortex ring possesses no azimuthal velocity component.

The aforementioned defined vortex ring velocities change the axial and radial velocities at each time step

$$u_{\text{ax}} = u_{\text{ax}} + \sum_{i=n}^{m} \alpha\, \varepsilon_i \cos(\text{i}\varphi + \varphi_i)\, u_{\text{e}}\, U_{\text{ax,ring}} \tag{8}$$

$$v_{\text{rad}} = v_{\text{rad}} + \sum_{i=n}^{m} \alpha\, \varepsilon_i \cos(\text{i}\varphi + \varphi_i)\, u_{\text{e}}\, V_{\text{rad,ring}} \tag{9}$$

The inflow forcing is based on the azimuthal modes where α is the force coefficient. The quantities m, n represent the lower and upper bounds of the modes. The random amplitude ε_i and phase φ_i differ at each time step between -1 and 1 and 0 and 2π.

The radial thickness of the inner and outer vortex ring is $r - r_{\text{ring}} = 0.0228\, R_{\text{e}}$ and $r - r_{\text{ring}} = 0.015\, R_{\text{e}}$ and the axial thickness of both rings is $x - x_{\text{ring}} = 0.015\, R_{\text{e}}$. The same forcing parameters, i.e. force coefficient α, number of modes $(m - n + 1)$, etc., are prescribed for both rings as in the reference study in [40].

A 10th-order polynomial fit is prescribed for the axial velocity distribution

$$u(r) = a_0 + \sum_{i=1}^{10} a_i \cdot r^i \tag{10}$$

at the nozzle exit which represents the inlet plane of the IEF case to match the mean nozzle exit velocity distribution of the FEF configuration. Table 1 shows the coefficients of Eq. (10) for the IEF problem. Moreover, the Crocco–Busemann relation [40] is used to map the nozzle exit density distribution of the FEF case onto the inlet of the IEF solution.

The maximum time averaged radial velocity $v_{\text{rad,max}}$ in the FEF configuration is less than $0.0056\, u_{\text{e}}$ in the nozzle exit plane. Thus, its impact is negligible in the inflow distribution of the IEF solution.

The comparison of the axial velocity and the density distributions of the conservation equation based solutions of the FEF configuration and the prescribed polynomial based distribution for the IEF case is shown in Fig. 3. The radial profiles obtained by Eq. (10) and the Crocco–Busemann relation for the IEF case almost perfectly match the mean nozzle exit distributions of the FEF case.

The flow problems possess a temperature ratio of $T_{\text{e}}/T_{\infty} = 3.1$, where T_{e} is the nozzle exit temperature for the FEF formulation and the jet inlet temperature for the IEF formulation. The Reynolds number $Re_{D_{\text{e}}} = \frac{\rho_{\text{e}} u_{\text{e}} D_{\text{e}}}{\eta_{\text{e}}}$ is defined based on the exit conditions, where ρ_{e} is the density, u_{e} is the average nozzle exit axial velocity

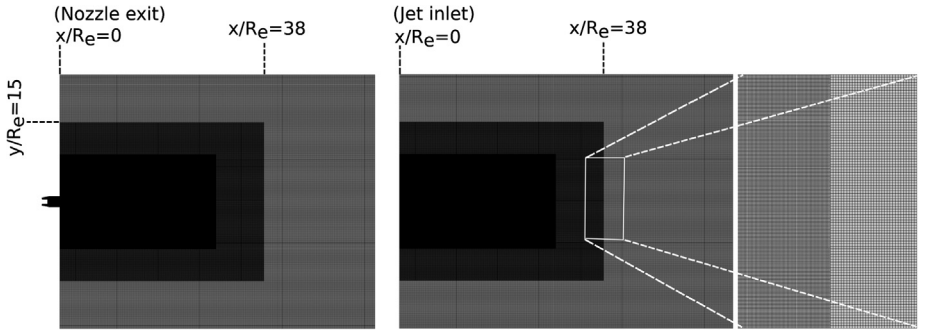

Fig. 4. Cartesian meshes for the free-exit-flow problem FEF where $x/R_e = 0$ is the nozzle exit (left) which also defines the jet inlet for the imposed-exit-flow problem IEF with an enlargement for the final refinement level jump (right).

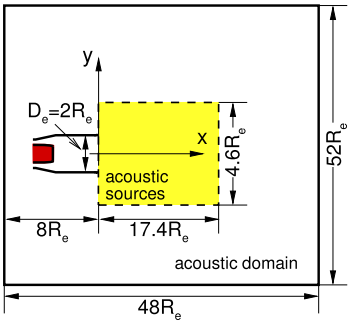

Fig. 5. Schematic of the acoustic computational domain in the $x-y$ plane, —— APE domain, – – – acoustic source region, R_e is the nozzle exit radius.

$$u_e = \frac{1}{A}\int \mathbf{u}\cdot\vec{n}\,\mathrm{d}A \tag{11}$$

$D_e = 2R_e$ the nozzle exit diameter, and η_e the dynamic viscosity. The Reynolds number for the FEF and IEF cases is $Re_{D_e} = 316,578$. The Mach number $M_j = \frac{u_e}{a_\infty}$ based on u_e and the ambient speed of sound a_∞ is $M_j = 0.12$ for both cases.

The LES meshes are generated by the parallelized Cartesian mesh generator [26]. The FEF grid contains 329×10^6 mesh cells, where the minimum cell length in the x-, y-, and z-directions is $\Delta x_{\min} = \Delta y_{\min} = \Delta z_{\min} = 0.00297\,D_e$. A grid convergence study in [30] showed that the current mesh resolution is sufficient to capture all the important features of the turbulent energy spectrum. The IEF grid contains 250×10^6 cells, where the grid is identical to the FEF case in the free-jet region. Fig. 4 depicts the Cartesian meshes used for the flow computations.

3.2. Acoustic field

Fig. 5 shows a schematic of the computational domain to determine the acoustic field. The noise source region extends by $17.4\,R_e$ in the axial direction and $4.6\,R_e$ in the sideline direction. The acoustic perturbation equations are solved on a domain that extends by $48R_e$ in the axial direction and $52\,R_e$ in the sideline direction. The minimum/maximum spatial step of $0.024\,R_e/0.53\,R_e$ in the sideline direction and the constant spacing of $0.024\,R_e$ in the jet direction of the source region result in approx. 108.5 million cells to resolve the acoustic field. The time step is $\Delta t = 0.011\,R_e/a_\infty$. Based on the summation by parts dispersion-relation-preserving scheme, the spectral resolution in the wavenumber space requires at least five points per wavelength λ. Consequently, on the present acoustic mesh, the maximum Strouhal number $St = f\,D_e/u_e$ based on the frequency f, the nozzle exit diameter D_e, and the mean axial exit velocity u_e is approximately $St_{\max} = 3$, where the mean wavelength $\overline{\lambda}$ is 5 times the grid spacing at a position $(x = 15\,R_e,\ y = 11\,R_e)$ of the acoustic domain. Table 2 summarizes the essential mesh and simulation parameters of the LES and APE computations.

4. Results

The flow field and the acoustic field of the free-exit-flow FEF and the imposed-exit-flow IEF configurations are analyzed. Note that the flow fields are discussed in great detail in [41], so that only a brief description of the FEF and IEF flow fields will be given. The differences in the development of the shear layers and the turbulent structures, which define the acoustic sources and as such the jet noise, will be evidenced since this information is necessary to understand the acoustic fields. The focus of the current discussion, however, will be on the FEF and IEF sound fields, which will be described at length. That is, while the investigation in [41] was on the flow field, the current analysis is new in the sense that the acoustic fields are addressed.

Table 2
Simulation features of the flow and acoustic simulations.

Mach number M	0.12
Reynolds number Re_{D_e}	316, 578
T_e/T_∞	3.1
Min. cell length	$\Delta x = 0.00297\, D_e$
Number of samples	2251
Simulation time	
Flow field	128 D_e/u_e
Acoustic field	638 D_e/a_∞
Mesh points	
Flow field FEF	329×10^6
Flow field IEF	250×10^6
Acoustic field	108×10^6

4.1. Flow field

The FEF and IEF flow computations are run for 128 D_e/u_e convective time units to reach a fully developed turbulent flow regime. For the averaged flow field and the turbulence statistics, 2251 LES snapshots within 70 D_e/u_e convective simulation time units are used. First, the instantaneous FEF and IEF flow fields are shown, then the time-averaged flow fields are qualitatively and quantitatively discussed. Finally, spectral analyses of turbulent quantities are investigated.

4.1.1. Instantaneous flow field

An overall impression of the jet flow field is given by the instantaneous contours of the vorticity component in the z-direction in Fig. 6. Compared to the IEF solution, the FEF solution shows a more perturbed flow distribution in the jet near field caused by the wall-bounded shear layer and the free-shear layer emanating from the centerbody. Therefore, no clear potential core exists in the FEF formulation. The IEF solution possesses two distinct shear layers right downstream of the exit. The inner shear layer is generated by the centerbody and the outer shear layer from the outer nozzle wall. These shear layers merge approx. five jet diameters downstream of the exit section. The comparison of the FEF and IEF solutions shows that the vortex ring forcing method, which is used to trigger the shear layer instabilities, can not perfectly model the free jet flow in the near field, since the perturbation of the inner shear layer, which determines the wake of the centerbody, is too local.

4.1.2. Time averaged flow field

The contours of the time-averaged axial velocity in the central $x-y$ plane are illustrated in Fig. 7. The FEF solution is characterized by a pronounced recirculation region right downstream of the centerbody inside the nozzle. This flow structure with an increased radial momentum exchange leads to a velocity distribution that determines the cone-like shape of the contours. Unlike the FEF configuration, the velocity contours of the IEF formulation result in a cylinder-like shape just downstream of the inflow plane. That is, although the axial velocity distributions of the FEF and IEF formulations in the $x/R_e = 0$ plane match, the flow development in the streamwise direction differs dramatically.

The temperature distributions of both solutions are plotted in Fig. 8. It is evident that although the exit distributions at $x/R_e = 0$ match for both solutions, further downstream, i.e. for $x/R_e > 0$, the temperature profiles differ due to the varying turbulent mixing in the jet near field. The FEF solution possesses a stronger temperature shear layer than the IEF solution caused by the turbulent wake generated by the centerbody which is missing in the IEF solution. Fig. 9 shows the turbulent kinetic energy $\mathrm{k} = \frac{1}{2}\left(\overline{u'^2} + \overline{v'^2} + \overline{w'^2}\right)$ distributions on the centerline, on the line in the shear layer region of the centerbody, and on the nozzle lip line. The distributions of the FEF solution on the centerline and on the line in the shear layer region of the centerbody in Figs. 9(a) and 9(b) have a much higher turbulent kinetic energy level close to the nozzle exit than the IEF solutions. That is, the turbulent structures, being shed from the centerbody, increase the turbulent fluctuations in the jet near field of the FEF solution, which is not perfectly modeled on the centerline and centerbody's shear layer in the IEF solution. The FEF distribution on the nozzle lip line in Fig. 9(c) possesses a higher increase than the IEF solution right downstream of the nozzle exit due to the delayed generation of turbulence by the forcing via vortex rings. However, both distributions almost match for $x/R_e > 10$. This means that the synthetically imposed flow distribution is a better model for the outer free-shear layer than the inner shear layer.

The two-point space-time correlation $R_{uu}(x,\tau) = \frac{<u'(x,\tau)u'(x+\Delta x,t+\tau)>}{<u'^2(x,t)>}$ distributions as a function of the streamwise distance Δx and the time shift τ in the centerbody's shear layer and outer free-shear layer at $x/R_e = 15$ are shown in Fig. 10. Again, the illustration shows that the IEF solution in the centerbody's shear layer decays more rapidly than the FEF solution, while the distributions in the outer free-shear layer almost match. Both solutions possess a Gaussian shape decay as discussed in the studies [30,42].

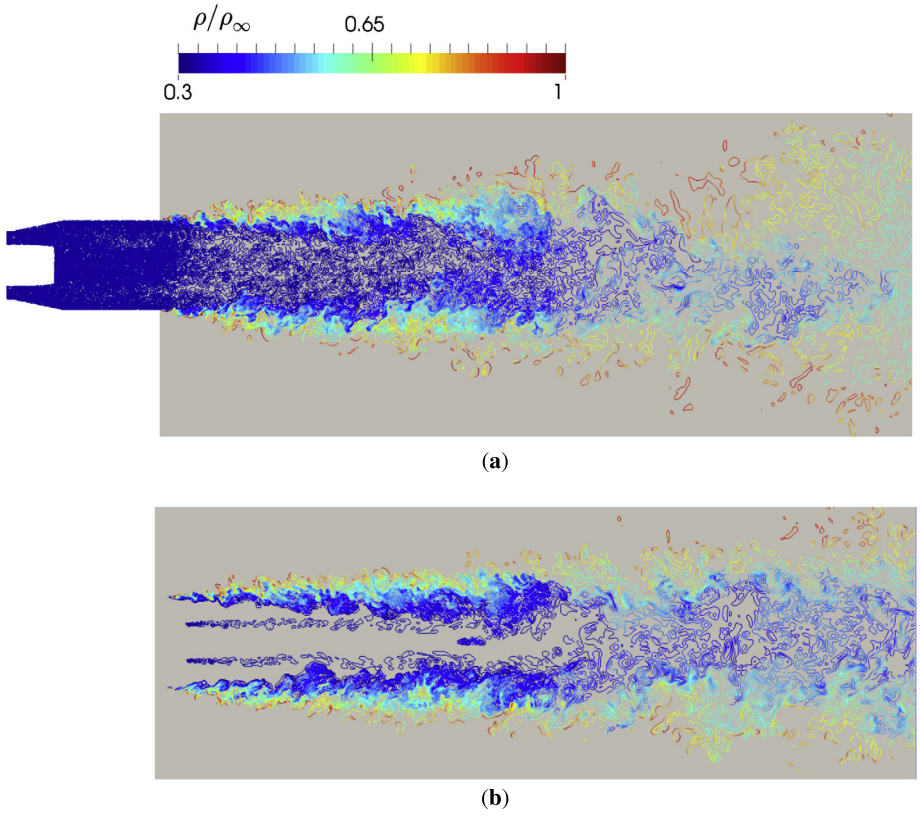

Fig. 6. Contours of the instantaneous distribution of the vorticity component in the z-direction color coded by the density in the central $x-y$ plane; the levels are chosen between min and max magnitudes where $-10 < \omega_z < 10$ for the FEF configuration and $-2 < \omega_z < 2$ for the IEF configuration; (a) free-exit-flow problem FEF, (b) imposed-exit-flow problem IEF.

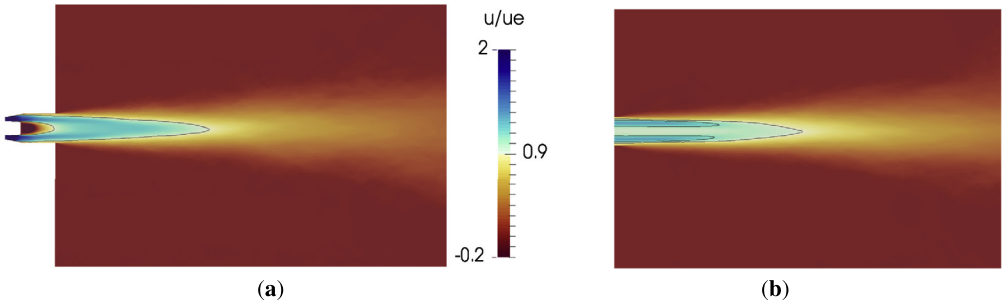

Fig. 7. Time averaged axial velocity contours u/u_e of the (a) free-exit-flow problem FEF, (b) imposed-exit-flow problem IEF.

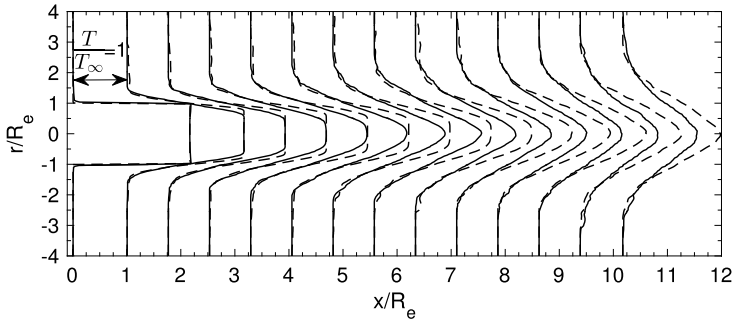

Fig. 8. Temperature distributions in the radial direction at several streamwise locations for (—) FEF, (– –) IEF.

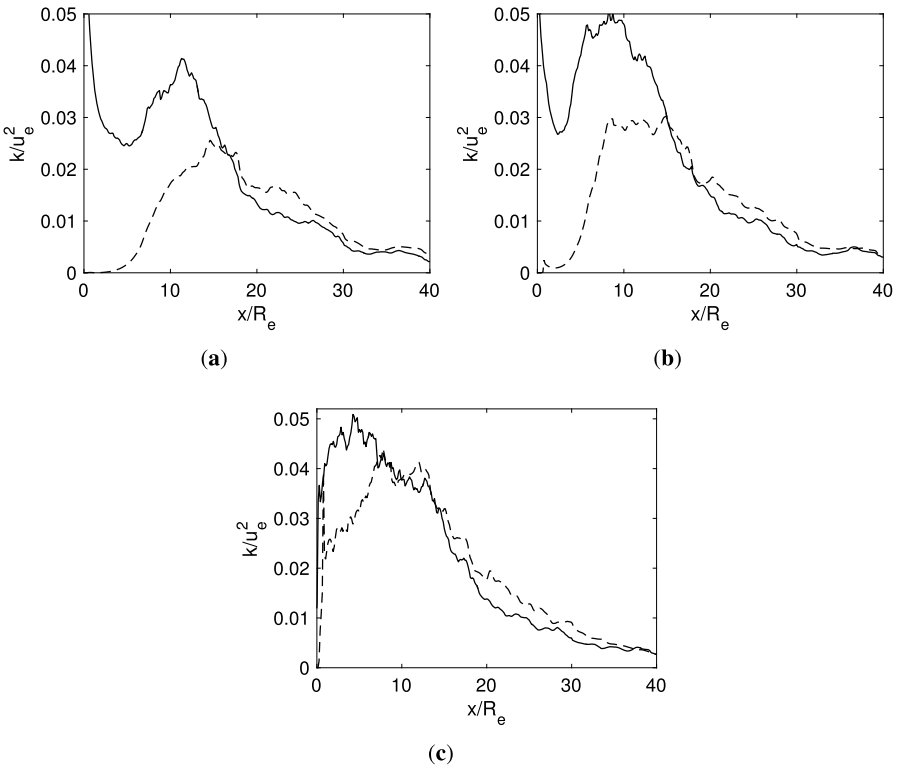

Fig. 9. Streamwise distribution of the turbulent kinetic energy k (a) on the centerline ($r/R_e = 0$), (b) on the line in the shear layer region of the centerbody ($r/R_e = 0.45$), and (c) on the lip line ($r/R_e = 1$) for the FEF (—) and the IEF case (– –).

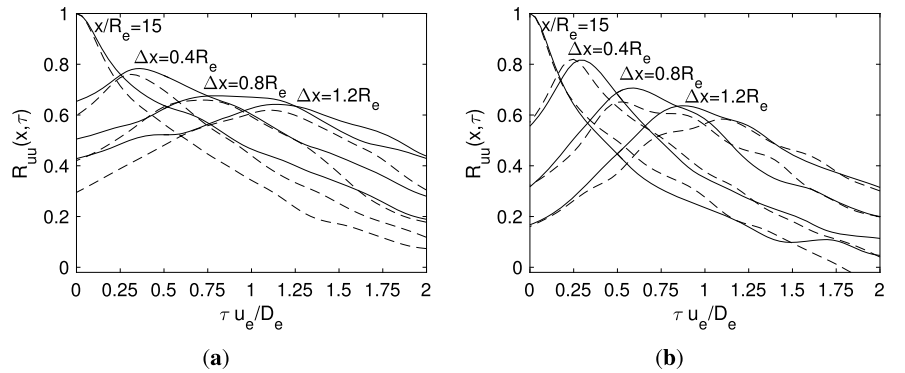

Fig. 10. Two-point space-time correlations of the fluctuating axial velocity component R_{uu} at the reference point $x/R_e = 15$ for several streamwise distances Δx along (a) the line in the shear layer region of the centerbody ($r/R_e = 0.45$) and (b) the nozzle lip line ($r/R_e = 1$) for the FEF (—) and the IEF case (– –).

4.1.3. Spectral analysis of the turbulent quantities in the jet near field

Next, the spectral content of the pressure fluctuations and the contours of the Fourier transformed auto-correlation $R_{uu}(\tau) = \frac{<u'(t)u'(t+\tau)>}{<u'^2(t)>}$ distributions of the axial velocity fluctuations are analyzed in the jet near field.

The power spectral density (PSD) distributions of the FEF and IEF cases are illustrated in Fig. 11. Two probe locations are considered, one in the centerbody's shear layer $x/R_e = 20$, $r/R_e = 0.45$ and one in the outer free-shear layer $x/R_e = 20$, $r/R_e = 1$. The IEF solution possesses a lower amplitude in the high-frequency range $St > 4$ in the centerbody's shear layer in Fig. 11(a) and the distributions in the outer free-shear layer in Fig. 11(b) almost match. This indicates that the vortex ring forcing method better mimics the spectral content of the wall-bounded shear layer in the nozzle exit plane than that of the free-shear layer. The contours of the Fourier transformed auto-correlations R_{uu} of the axial velocity component are illustrated in Fig. 12. The IEF solution at $x/R_e = 10$ in Fig. 12(b) shows a less pronounced high-frequency spectral content in the region $-2 < r/R_e < 2$ than the FEF solution in Fig. 12(a), which is related to the less pronounced turbulent mixing in this cross section. Further downstream at $x/R_e = 20$, both jets reveal a qualitatively almost likewise distribution in Figs. 12(c) and 12(d).

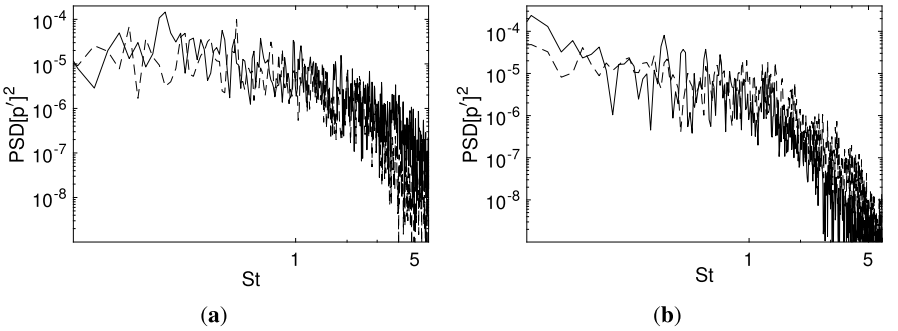

Fig. 11. Power spectral density (PSD) distributions of the pressure fluctuations in (a) the centerbody's shear $x/R_e = 20$, $r/R_e = 0.45$ and (b) the outer shear layer $x/R_e = 20$, $r/R_e = 1$ for the FEF (—) and the IEF case (– –).

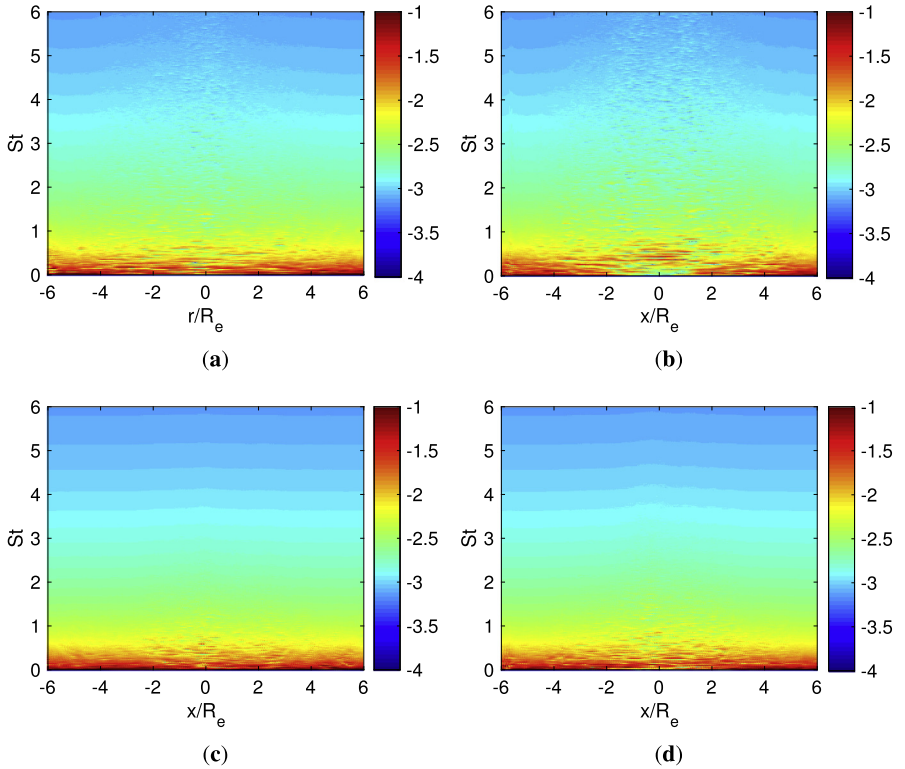

Fig. 12. Contours of the Fourier transformed auto-correlations in the radial direction (a) at $x/R_e = 10$ for the FEF case, (b) at $x/R_e = 10$ for the IEF case, (c) at $x/R_e = 20$ for the FEF case, (d) at $x/R_e = 20$ for the IEF case.

4.2. Acoustic field

The analysis of the results of the acoustic field contains two parts. In the first part, the overall noise fields of the FEF and IEF configurations are juxtaposed to emphasize the influence of the exit conditions on the noise radiation. In the second part, the analysis focuses on the impact of the various noise sources on the sound field.

4.2.1. Impact of the exit conditions on the overall noise field

First, the impact of the FEF and IEF configurations on the various noise sources is analyzed. The sound sources are determined by the unsteady eddy motion and the momentum intrusion of convecting turbulence [43] which varies for the individual jet configurations.

In Fig. 13, the contours of the acoustic pressure in the near field of the jet are illustrated in the range $|p'/\rho_0 a_0^2| \leq 5 \times 10^{-6}$. The IEF configuration in Fig. 13(b) obviously generates less noise than the FEF configuration in Fig. 13(a), since the pronounced vortical structures generated by the centerbody are hardly modeled by the IEF formulation. The lower acoustic energy in the IEF jet is due to the lower turbulent kinetic energy distribution, as shown in Fig. 9. The large amplitude, which has a wavelength of approximately $30\,R_e$, corresponds to the non-dimensional frequency $St = f D_e/U_e = 0.56$. In this

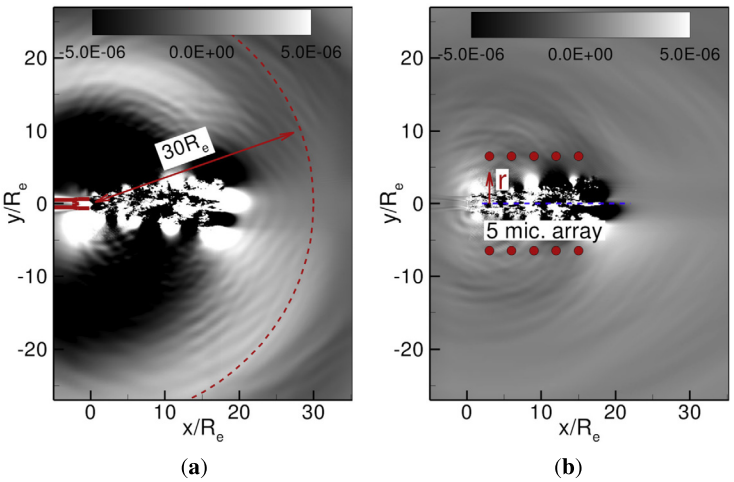

Fig. 13. Acoustic pressure contours determined for the configurations (a) FEF and (b) IEF, the range of the acoustic pressure is normalized by $\rho_0 a_0^2$ is $|p'/\rho_0 a_0^2| \leq 5 \times 10^{-6}$; the five-microphone array is located at a radial position $r/R_e = 6$ from the centerline.

frequency range, the turbulent fluctuations associated with the entropy source q_e are much more pronounced for the FEF than the IEF configuration. The details of the sound spectra are analyzed next, and the impact of the FEF and IEF formulations is discussed for all the source terms. That is, the distributions of the acoustic pressure signals determined on the five-microphone array at a radial position $r/R_e = 6$ shown in Fig. 13(b) are analyzed. The sound spectra determined by all the source terms in Fig. 14 show the variation of the source contribution to the acoustic generation in the near field. The acoustic field of the IEF configuration shows almost similar decaying sound spectra at all streamwise locations $3 \leq x/R_e \leq 15$ with amplitudes increasing by 10 dB in the streamwise direction at low frequencies $St < 0.4$. The FEF configuration, however, possesses, on the one hand, higher amplitude sound spectra than the IEF formulation and, on the other hand, a different qualitative behavior for $x/R_e \leq 9$. This difference is defined by the increasing and decreasing distribution in the frequency range $0.2 \leq St \leq 0.8$. It will be shown that this variation is strongly determined by the entropy source distributions. The spectral peak changes from a higher frequency $St = 0.45$ for $x/R_e \leq 9$ to a lower frequency $St = 0.04$ at the position $x/R_e = 15$. The IEF configuration does not yield the same broadband distribution since the acoustic sources of the excess density ρ_e of the IEF solution do not match the same level as in the FEF solution due to the delayed transition. The sound spectra in the near field indicate that the forcing used for the prescribed inflow profile does not generate the turbulent fluctuations coupled with the thermal expansion and the entropy variation. The forcing by velocity fluctuations does not suffice to mimic the overall character of the acoustic field generated by the real nozzle flow.

4.2.2. Impact of the exit conditions on the source terms

The following discussion focuses on the analysis of the impact of the exit conditions on the distributions of the decomposed acoustic sources in the APE-4 system. The source components are divided into three parts, i.e. the momentum $\mathbf{q}_m$, the entropy q_e, and the nonlinear q_c sources in Eqs. (1) and (2). The momentum source $\mathbf{q}_m$ in Eq. (5) contains besides the fluctuations of the Lamb vector components, i.e. the vortex sound source, the thermodynamic fluctuations, and the nonlinear effects of the turbulent kinetic energy. Considering the result of the hot-jet analysis in [9], in which the temperature gradient was a major sound source contributor, the entropy source term is expected to strongly contribute to the noise generation.

In Fig. 15, the axial development of the sound sources is presented by the distributions of the root-mean-square (rms) values of the acoustic source terms in Eqs. (3), (4), and (5). On the outer shear layer $r/R_e = 1$, the source terms containing the heat components, i.e. the source q_c in Fig. 15(a) and the source q_e in Fig. 15(b), are highly intensified immediately downstream of the nozzle exit.

On the centerline $r/R_e = 0$, the strong increase of the q_c and q_e sources is shifted downstream, i.e. the rms peaks occur at higher x/R_e locations since the turbulent mixing has to grow in the streamwise direction. It is evident that this shift of the q_c and q_e peaks in the downstream direction is more pronounced for the IEF than the FEF formulations. Moreover, the maxima of the FEF solutions are always greater than the IEF maxima. Unlike the q_c and q_e findings, the q_m distributions of the FEF and IEF formulations are not qualitatively alike. The q_m distributions of the FEF case in Fig. 15(c) almost monotonically decrease in the streamwise direction on the centerline and on the outer shear layer, while the IEF solutions possess a local extremum downstream of the nozzle exit plane. It goes without saying that this varying behavior is due to the lower turbulent mixing intensity initialized by the vortex ring forcing method. Since the sound sources q_c, q_e, and q_m determine the acoustic field, a large quantitative difference of the FEF and IEF sound fields is determined in Fig. 14. It is evident from Fig. 16 that the overall sound pressure level of the FEF configuration is higher than that of the IEF case. This result is true for the individual source terms q_c, q_e, and q_m and consequently also for the combination of all sources. The

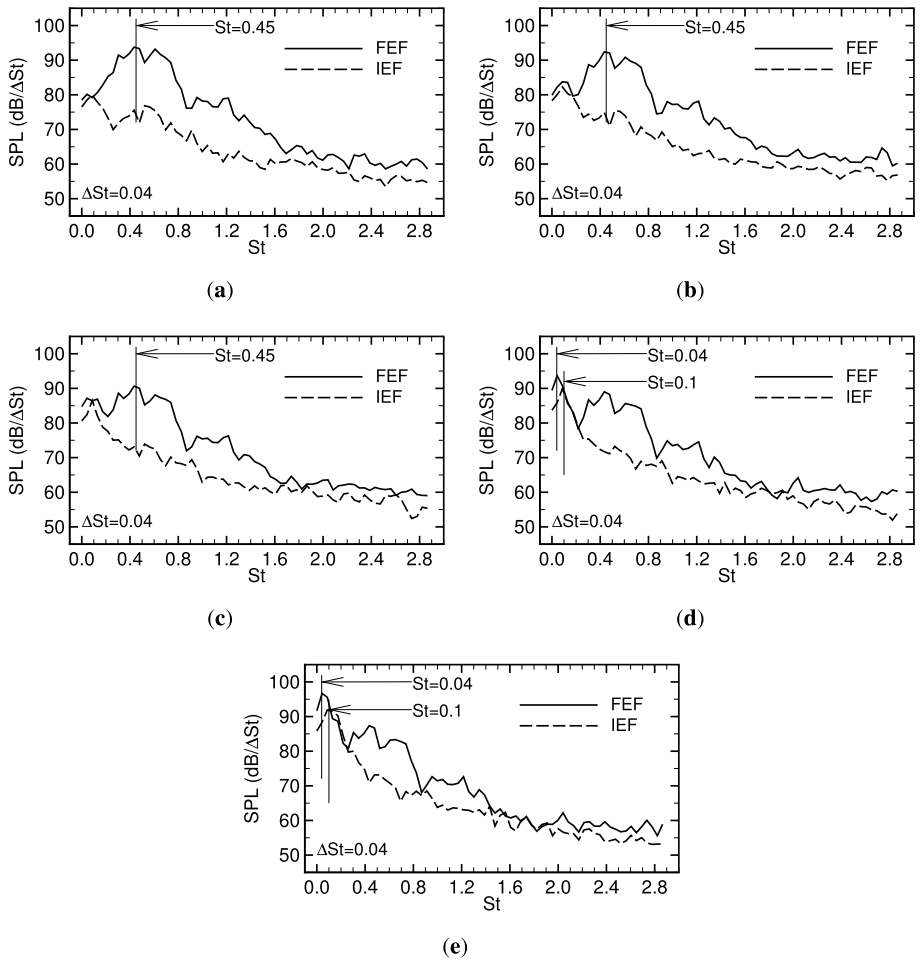

Fig. 14. Sound spectra determined by all acoustic source terms for the configurations FEF (——) and IEF (– – –) in the near field at a radial position $r/R_e = 6$ for the axial coordinates (a) $x/R_e = 3$, (b) $x/R_e = 6$, (c) $x/R_e = 9$, (d) $x/R_e = 12$, and (e) $x/R_e = 15$.

qualitative behavior of the q_e and q_m sources is different for the FEF and IEF formulations. The q_e distribution of the FEF solution decreases, while that of the IEF solution increases with the streamwise position. This seems to be caused by the pronounced downstream shift of the peak on the centerline illustrated in Fig. 15(b). The qualitative difference in the q_m distributions in Fig. 16(b) is less dramatic since both solutions increase for $x/R_e \geq 8$. Only just downstream of the nozzle exit, the FEF solution shows unlike the IEF solution a plateau-like distribution. The comparison with Fig. 15(c) indicates that this discrepancy is again caused by the varying development on the centerline. The distributions of the q_c term possess the same tendency. The amplitudes of the OASPL for the FEF and IEF solutions grow with a slightly higher slope for the FEF case. Note that in the FEF and IEF formulations, the entropy source q_e is the leading term of the overall sound pressure level in the near field shown in Fig. 16. The OASPL difference between two configurations FEF and IEF is increased up to 12 dB in the sideline acoustics where the entropy source possesses the dominant impact on the noise generation. In the IEF solution, the temperature and the density fluctuations have to be excited by the jet forcing and augmented by the mixing process. They show a delayed growth in the streamwise direction without reaching the FEF amplitudes in the near-field region $x/R_e \leq 15$. Fig. 17 shows the acoustic contribution of the various noise sources on the sound spectra. In the left column, the sound spectra of the sideline acoustics $x/R_e = 3$ are presented and in the right column, the distributions of the downstream acoustics $x/R_e = 15$ are illustrated. The acoustic contribution by the nonlinear source q_c in Fig. 17(a) shows that the sideline acoustic generation of the FEF formulation is higher than that of the IEF case over the complete frequency range $St \leq 2.8$. The FEF and IEF downstream sound spectra are almost alike except in the very low frequency range.

The impact of the high temperature of the jet on the noise is evidenced by the entropy source q_e in Fig. 17(b). For the FEF configuration, the sound generation in the sideline direction results in a much higher acoustic radiation than the IEF configuration. This varying qualitative and quantitative behavior of the FEF and IEF solutions diminishes in the streamwise direction which is shown at $x/R_e = 15$ in Fig. 17(b). As illustrated by the distributions of the OASPL in Fig. 16, the dominant acoustic source is the strong temperature or density gradients so that the sound spectrum from the entropy source q_e almost matches the full source acoustic spectra shown in Fig. 14(a).

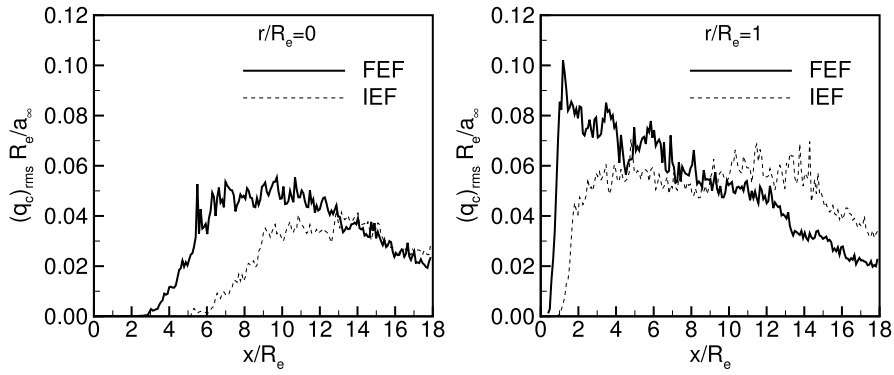

(**a**)

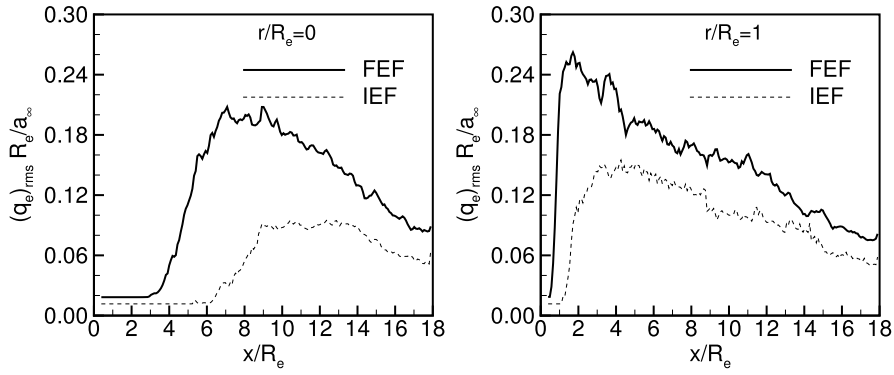

(**b**)

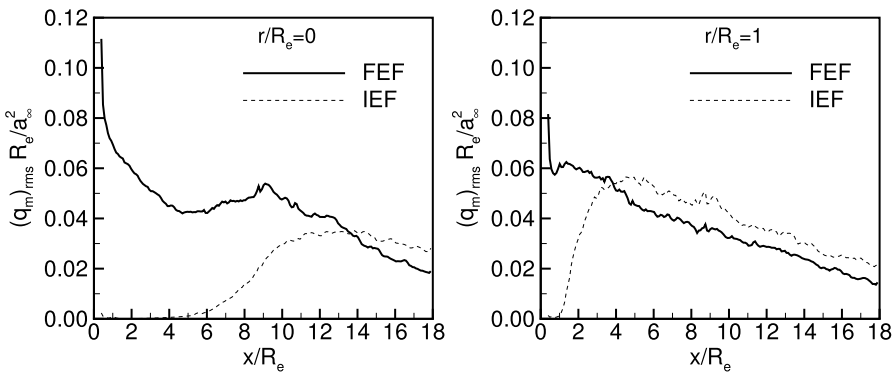

(**c**)

Fig. 15. Axial distributions of the rms values of the acoustic sources determined on the centerline (left column) and on the free-shear layer $r/R_e = 1$ (right column), (a) continuity source q_c in Eq. (3), (b) entropy source q_e in Eq. (4), (c) momentum source $|\mathbf{q}_m|$ in Eq. (5).

The momentum source in Fig. 17(c) has a minor impact on the sideline acoustics than the entropy source. Due to the vortical structures shed from the centerbody, the FEF configuration has a peak at $St = 0.6$ in the distribution of the $\mathbf{q}_m$ source term [15], which is also visible as a second peak in the distribution of all source terms in Fig. 14(a). At the downstream position $x/R_e = 15$, the acoustic contribution of the momentum source becomes the dominant term in the low-frequency range with a peak near $St \approx 0.04$ (Fig. 14(e), Fig. 17(c)). The IEF configuration possesses a lower, qualitatively similar q_m sound spectrum distribution. Only the pronounced peak in the sideline direction caused by the free-shear layer emanating from the centerbody is missing.

The FEF solution generates strong broadband acoustics in the frequency range $St < 0.8$, with a peak located at $St = 0.45$. The turbulent flow includes a high-intensity entropy source that describes the acoustic contribution of the excess density ρ_e in Eq. (4). The entropy source consists of two parts, i.e. the local derivative of the excess density $q_{et} = -\frac{\partial \rho_e}{\partial t}$ and the spatial rate of change of the product of the excess density and the mean velocity $q_{es} = -\nabla \cdot (\rho_e \overline{\mathbf{u}})$. Due to the dominance of the q_e term in the sound spectra the noise generation of the individual parts is illustrated in Fig. 18 for the FEF and IEF solutions

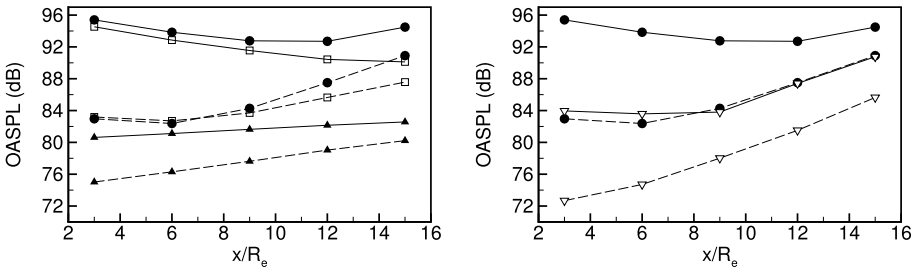

Fig. 16. Overall sound pressure level determined for the configurations FEF (——) and IEF (– – –) in the near field of a radial position $r/R_e = 6$ based on various combinations of the acoustic source terms, (a) all source terms (•), q_c (▲), and q_e (□), (b) all source terms (•) and $\mathbf{q}_m$ (▽).

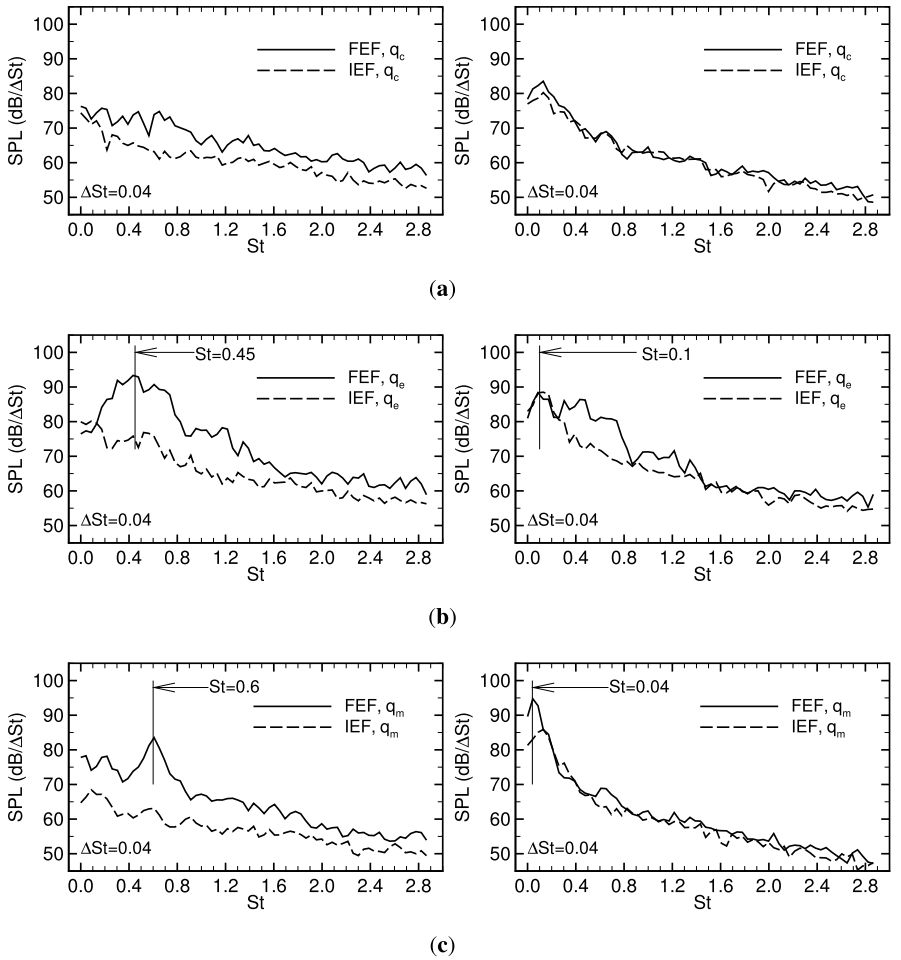

Fig. 17. Sound spectra determined by the individual acoustic source terms for the configurations FEF (——) and IEF (– – –) in the near field at a radial position $r/R_e = 6$ and the streamwise coordinates of $x/R_e = 3$ (left column) and $x/R_e = 15$ (right column), (a) source q_c in Eq. (3), (b) source q_e in Eq. (4), (c) source $|\mathbf{q}_m|$ in Eq. (5).

at the axial positions $x/R_e = 3$ and $x/R_e = 15$. In Figs. 18(a) and 18(c), the sound generation of q_{et} is more pronounced than that of the total entropy term q_e, i.e. the SPL of the total entropy source is determined by partial acoustic source cancellation of q_{et} and q_{es}. The sound spectra of q_{et} and q_{es} show a similar frequency dependence since both terms are dominated by the turbulent fluctuations of the excess density ρ_e. The comparison of the FEF and IEF solutions, i.e. Figs. 18(a) and 18(b) and Figs. 18(c) and 18(d), shows the major difference to occur in the sideline direction. Further downstream at $x/R_e = 15$, the mixing process has excited the density fluctuations, which determine the q_{et} and q_{es} sources, so that the FEF and IEF results almost match. In the near field at $x/R_e = 3$, the density fluctuations in the IEF solution, which have to be triggered

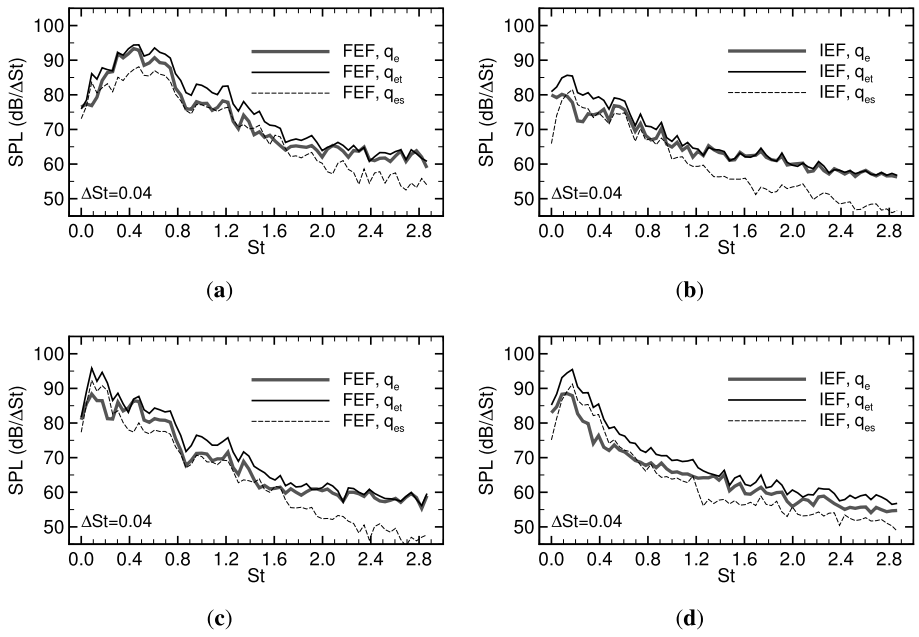

Fig. 18. Sound spectra determined by the entropy source q_e defined in Eq. (4), where $q_{et} = -\frac{\partial \rho_e}{\partial t}$ and $q_{es} = -\nabla \cdot (\rho_e \overline{\mathbf{u}})$; (a) the FEF solution at $r/R_e = 6$, $x/R_e = 3$, (b) the IEF solution at $r/R_e = 6$, $x/R_e = 3$, (c) the FEF solution at $r/R_e = 6$, $x/R_e = 15$, (d) the IEF solution at $r/R_e = 6$, $x/R_e = 15$.

by the velocity field, are too low, so that the SPL level compared to the FEF solution is clearly underpredicted. Since the q_e term dominates the near-field acoustics, it is the lack of density fluctuations in the imposed-exit-flow formulation that causes the pronounced differences in the FEF and IEF acoustics.

In conclusion, the FEF and IEF configurations possess clearly different sideline acoustic fields. That is, even the qualitative behavior of the sound spectrum of the FEF distribution is not obtained by the IEF formulation. This difference occurs since the excess density term $\rho_e = (\rho - \overline{\rho}) - (p - \overline{p})/\overline{a^2}$, which dominates the acoustic entropy source, is not sufficiently generated by the vortex-ring-forcing method in the IEF solution. In the downstream direction, the FEF and IEF sound spectra approach each other. Furthermore, the momentum source dominates the sound spectrum in the low-frequency range.

5. Summary

The flow field and the acoustic field of turbulent hot jets are computed by a hybrid large-eddy simulation/computational aeroacoustics method for two formulations. First, the free-exit-flow (FEF) formulation is considered, in which the flow inside the nozzle is part of the overall flow field computation, i.e. the nozzle exit flow is determined by the solution of the discretized conservation equations. Second, in the imposed-exit-flow (IEF) formulation, the time-averaged flow distributions of the free-exit-flow solution are imposed in the nozzle exit cross section, i.e. on the inflow plane, plus two vortex rings for the wall-bounded and free-shear layer to trigger the shear layer instabilities. It goes without saying that the variations of the flow field and the acoustic field in the FEF and IEF solutions are related to the current nozzle geometry.

The differences in the FEF and IEF flow field are evidenced by the varying turbulent mixing in the jet near field. The FEF solution has a clearly higher turbulent kinetic energy level just downstream of the nozzle exit than the IEF solution. This is due to the fact that, unlike the wall-bounded shear layer, the flapping motion of the free-shear layer downstream of the centerbody of the nozzle is not generated by the vortex ring forcing method. This results in a different jet pattern in the near field, i.e. the FEF flow resembles a converging and the IEF flow a cylindrical streamtube.

The analysis of the acoustic fields of the FEF and IEF formulations is based on the solution of the acoustic perturbation equations. The closer to the nozzle exit, the more pronounced are the quantitative differences in the FEF and IEF solutions. The total overall sound pressure level possesses the same qualitative behavior for the FEF and IEF formulations, while the distributions of the entropy source term, which is the dominant source in the jet near field, show an opposing trend. This clear discrepancy is caused by the noise sources generated by the density and pressure fluctuations which are not perfectly captured by the IEF formulation due to the delayed transition. Further downstream, the momentum source term dominates the sound spectra in the low-frequency range and the differences in the FEF and IEF acoustic fields decay.

Acknowledgements

The research was funded from the European Community's Seventh Framework Programme (FP7, 2007–2013) PEOPLE program under the grant agreement No. FP7-290042 (COPAGT project). The authors gratefully thank the Gauss Centre for

Supercomputing (GCS) for providing computing time for a GCS Large-Scale Project on the GCS share of the supercomputer JUQUEEN [44] at the Jülich Supercomputing Centre (JSC) and High Performance Computing Center Stuttgart (HLRS). GCS is the alliance of the three national supercomputing centres HLRS (Universität Stuttgart), JSC (Forschungszentrum Jülich), and LRZ (Bayerische Akademie der Wissenschaften) in Germany, funded by the German Federal Ministry of Education and Research (BMBF) and the German State Ministries for Research of Baden-Württemberg (MWK), Bayern (StMWFK), and Nordrhein-Westfalen (MIWF).

References

[1] K.B.M.Q. Zaman, Effect of Nozzle Exit Conditions on Subsonic Jet Noise, AIAA Paper, 2011–2704, 2011.
[2] N. Andersson, L.-E. Eriksson, L. Davidson, Effects of Inflow Conditions and Subgrid Model on LES for Turbulent Jets, AIAA Paper, 2005–2925, 2005.
[3] F. Keiderling, L. Kleiser, C. Bogey, Numerical study of eigenmode forcing effects on jet flow development and noise generation mechanisms, Phys. Fluids 21 (4) (2009) 045106.
[4] C. Bogey, C. Bailly, Influence of nozzle-exit boundary-layer conditions on the flow and acoustic fields of initially laminar jets, J. Fluid Mech. 663 (2010) 507–538.
[5] C. Bogey, O. Marsden, Identification of the effects of the nozzle-exit boundary-layer thickness and its corresponding Reynolds number in initially highly disturbed subsonic jets, Phys. Fluids 25 (5) (2013) 055106.
[6] D.J. Bodony, S.K. Lele, Current status of jet noise predictions using large-eddy simulation, AIAA J. 46 (2) (2008) 364–380.
[7] D.J. Bodony, S.K. Lele, On using large-eddy simulation for the prediction of noise from cold and heated turbulent jets, Phys. Fluids 17 (8) (2005) 085103.
[8] M. Shur, P. Spalart, M. Strelets, Noise prediction for increasingly complex jets. Part II: applications, Int. J. Aeroacoust. 4 (3) (2005) 247–266.
[9] S.R. Koh, W. Schröder, M. Meinke, Turbulence and heat excited noise sources in single and coaxial jets, J. Sound Vib. 329 (7) (2010) 786–803.
[10] K. Viswanathan, Aeroacoustics of hot jets, J. Fluid Mech. 516 (2004) 39–82.
[11] M. Gloor, S. Bühler, L. Kleiser, Transition to turbulence and noise radiation in heated coaxial jet flows, Phys. Fluids 28 (4) (2016) 044103.
[12] J. Panda, R.G. Seasholtz, K.A. Elam, A.F. Mielke, D.G. Eck, Effect of Heating on Turbulent Density Fluctuations and Noise Generation from High Speed Jets, AIAA Paper, 2004–3016, 2004.
[13] V.F. Dippold, L.E. Foster, M.R. Wiese, Computational analyses of offset-stream nozzles for noise reduction, J. Propuls. Power 25 (1) (2009) 204–217.
[14] B. Henderson, T. Norum, J. Bridges, An MDOE Assessment of Nozzle Vanes for High Bypass Ratio Jet Noise Reduction, AIAA Paper, 2006–2543, 2006.
[15] M.O. Cetin, S.R. Koh, M. Meinke, W. Schröder, Numerical analysis of the impact of the interior nozzle geometry on low Mach number jet acoustics, Flow Turbul. Combust. 98 (2) (2017) 417–443.
[16] C. Brown, J. Bridges, B. Henderson, Offset Stream Technology Test – Summary of Results, AIAA Paper, 2007–3664, 2007.
[17] D. Papamoschou, F. Liu, Aerodynamics of fan flow deflectors for jet noise suppression, J. Propuls. Power 24 (3) (2008) 437–445.
[18] D. Papamoschou, Fan flow deflection in simulated turbofan exhaust, AIAA J. 44 (12) (2006) 3088–3097.
[19] A.D. Johnson, J. Xiong, S. Rostamimonjezi, F. Liu, D. Papamoschou, Aerodynamic and Acoustic Optimization for Fan Flow Deflection, AIAA Paper, 2011–1156, 2011.
[20] J. Xiong, F. Liu, D. Papamoschou, Aerodynamic performance of fan-flow deflectors for jet-noise reduction, J. Propuls. Power 28 (4) (2012) 728–738.
[21] J. Xiong, P. Nielsen, F. Liu, D. Papamoschou, Computation of high-speed coaxial jets with fan flow deflection, AIAA J. 48 (10) (2010) 2249–2262.
[22] J.P. Boris, F.F. Grinstein, E.S. Oran, R.L. Kolbe, New insights into large eddy simulation, Fluid Dyn. Res. 10 (4–6) (1992) 199–228.
[23] M. Meinke, W. Schröder, E. Krause, T. Rister, A comparison of second-and sixth-order methods for large-eddy simulations, Comput. Fluids 31 (4) (2002) 695–718.
[24] D. Hartmann, M. Meinke, W. Schröder, A strictly conservative Cartesian cut-cell method for compressible viscous flows on adaptive grids, Comput. Methods Appl. Mech. Eng. 200 (9) (2011) 1038–1052.
[25] L. Schneiders, C. Günther, M. Meinke, W. Schröder, An efficient conservative cut-cell method for rigid bodies interacting with viscous compressible flows, J. Comput. Phys. 311 (2016) 62–86.
[26] A. Lintermann, S. Schlimpert, J. Grimmen, C. Günther, M. Meinke, W. Schröder, Massively parallel grid generation on HPC systems, Comput. Methods Appl. Mech. Eng. 277 (2014) 131–153.
[27] L. Schneiders, D. Hartmann, M. Meinke, W. Schröder, An accurate moving boundary formulation in cut-cell methods, J. Comput. Phys. 235 (2013) 786–809.
[28] A. Pogorelov, M. Meinke, W. Schröder, Cut-cell method based large-eddy simulation of tip-leakage flow, Phys. Fluids 27 (7) (2015) 075106.
[29] S. Schlimpert, A. Feldhusen, J. Grimmen, B. Roidl, M. Meinke, W. Schröder, Hydrodynamic instability and shear layer effects in turbulent premixed combustion, Phys. Fluids 28 (1) (2016) 017104.
[30] M.O. Cetin, V. Pauz, M. Meinke, W. Schröder, Computational analysis of nozzle geometry variations for subsonic turbulent jets, Comput. Fluids 136 (2016) 467–484.
[31] J.B. Freund, Proposed inflow/outflow boundary condition for direct computation of aerodynamic sound, AIAA J. 35 (4) (1997) 740–742.
[32] R. Ewert, W. Schröder, Acoustic perturbation equations based on flow decomposition via source filtering, J. Comput. Phys. 188 (2) (2003) 365–398.
[33] S.R. Koh, G. Geiser, W. Schröder, Reformulation of Acoustic Entropy Source Terms, AIAA Paper, 2011–2927, 2011.
[34] J.J. Markham, Second-order acoustic fields: streaming with viscosity and relaxation, Phys. Rev. 86 (4) (1952) 497.
[35] C.K.W. Tam, J.C. Webb, Dispersion-relation-preserving finite difference schemes for computational acoustics, J. Comput. Phys. 107 (2) (1993) 262–281.
[36] F.Q. Hu, M.Y. Hussaini, J.L. Manthey, Low-dissipation and low-dispersion Runge–Kutta schemes for computational acoustics, J. Comput. Phys. 124 (1) (1996) 177–191.
[37] W. Schröder, R. Ewert, LES-CAA coupling, in: Large-Eddy Simulations for Acoustics, Cambridge University Press, 2005.
[38] R. Ewert, W. Schröder, On the simulation of trailing edge noise with a hybrid LES/APE method, J. Sound Vib. 270 (3) (2004) 509–524.
[39] C. Siewert, R.P.J. Kunnen, W. Schröder, Collision rates of small ellipsoids settling in turbulence, J. Fluid Mech. 758 (2014) 686–701.
[40] C. Bogey, C. Bailly, Computation of a high Reynolds number jet and its radiated noise using large eddy simulation based on explicit filtering, Comput. Fluids 35 (10) (2006) 1344–1358.
[41] M.O. Cetin, M. Meinke, W. Schröder, Numerical analysis of the impact of exit conditions on low Mach number turbulent jets, Int. J. Heat Fluid Flow 67 (2017) 1–12.
[42] N.K. Depuru Mohan, A.P. Dowling, S.A. Karabasov, H. Xia, O. Graham, T.P. Hynes, P.G. Tucker, Acoustic sources and far-field noise of chevron and round jets, AIAA J. 53 (9) (2015) 2421–2436.
[43] C.K.W. Tam, Jet noise: since 1952, Theor. Comput. Fluid Dyn. 10 (1) (1998) 393–405.
[44] J.S. Centre, Juqueen: IBM Blue Gene/Q Supercomputer System at the Jülich Supercomputing Centre, J. Large-Scale Res. Facil. 1 (A1) (2015), https://doi.org/10.17815/jlsrf-1-18.